

Multi-Flow: Multi-View-Enriched Normalizing Flows for Industrial Anomaly Detection

Mathis Kruse Bodo Rosenhahn

Institute for Information Processing, L3S - Leibniz University Hannover

kruse@tnt.uni-hannover.de

Abstract

With more well-performing anomaly detection methods proposed, many of the single-view tasks have been solved to a relatively good degree. However, real-world production scenarios often involve complex industrial products, whose properties may not be fully captured by one single image. While normalizing flow based approaches already work well in single-camera scenarios, they currently do not make use of the priors in multi-view data. We aim to bridge this gap by using these flow-based models as a strong foundation and propose Multi-Flow, a novel multi-view anomaly detection method. Multi-Flow makes use of a novel multi-view architecture, whose exact likelihood estimation is enhanced by fusing information across different views. For this, we propose a new cross-view message-passing scheme, letting information flow between neighboring views. We empirically validate it on the real-world multi-view data set Real-IAD [54] and reach a new state-of-the-art, surpassing current baselines in both image-wise and sample-wise anomaly detection tasks.

1. Introduction

During any manufacturing process, a myriad of possible production errors inevitably lead to faults and costly replacement of products. The field of industrial anomaly detection aims to solve this problem, by detecting anomalies in these products. When detected early on in the manufacturing chain, this may successfully cut down on material and manual inspection cost, making the entire process more efficient. As defects are not definable a priori and usually only occur very rarely, anomaly detection focuses on semi-supervised training schemes, where algorithms have access to normal data only [5]. This normal and anomaly-free data is often more widely available and can be more easily collected during already-running process pipelines.

Most image-based frameworks currently assume that only one static camera position is sufficient to determine

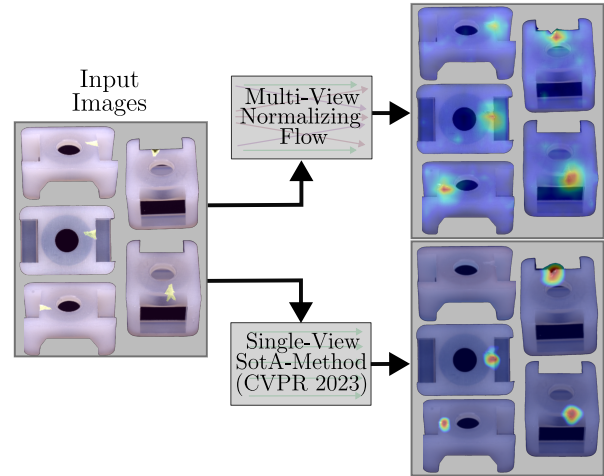


Figure 1. Overview of the multi-view enriched normalizing flow compared to SimpleNet [38]. Multiple views of an object (with anomalies marked) get processed by the normalizing flow. Where single-view methods may struggle, *Multi-Flow* detects anomalies irrespective of the objects view point.

whether an object is an anomaly [5, 7, 71]. Here, the most-used perspective is a birds-eye view of the object, as it is frequently used in data sets such as MVTEC AD [5], MVTEC Loco [7] and the Visual Anomaly Dataset (VisA) [71]. This may neglect any three-dimensional or hidden information, which is only inferrable from other views, or by combining many views of one object. The recently published data set Real-IAD [54] serves as an example of this new tasks. Here, an object is now photographed from five different view-points, with one of them being the birds-eye view that is also present in other data sets. While established methods may also work on images outside of the regular birds-eye camera pose, they fail to fuse the multi-view information to make an informed decision about the entire object [38, 48].

Existing multi-view methods, such as OmniAD [69] or SplatPose [31] use novel-view synthesis methods to model an object. However, they require up to hundreds of views to capture the 3D information. Even then, they assume the ex-

istence of a perfect "normal" model, from which all anomalies deviate. This is a crucial shortcoming, as it does not model any variance in texture or shape.

In this work, we propose *Multi-Flow*, which manages to model a distribution across hundreds of different objects, each containing far fewer views (e.g. five for Real-IAD [54] compared to roughly two hundred for MAD [69]). This is achieved by fusing information across different views of an object using an architecture based on normalizing flows. Normalizing flows have been shown to learn distributions of samples very well, which also makes them suitable to learn the anomaly-free normal distribution of our multi-view objects [28, 49, 50]. For this, we specifically design a multi-view coupling block network that uses message-passing and aggregation of the multi-view data. We further propose to leverage a data augmentation and conditioning scheme, to regularize and stabilize the training process. Our method achieves state-of-the-art performance in the multi-view anomaly detection task on Real-IAD when detecting anomalies both at an image and at the instance level, while still achieving competitive results in segmenting the anomalies. This makes us able to detect anomalies irrespective of the view they are in, as visualized in Fig. 1. Here, SimpleNet [38], which does not model multi-view information, can be seen struggling with detecting all anomalies. We also conduct several ablation studies to additionally motivate our choices of architecture and training procedure.

To summarize, our **contributions** include

- We propose *Multi-Flow* for multi-view anomaly detection and reach a new state of the art for detection tasks on Real-IAD
- We design a multi-view-aware coupling block for efficient fusion of multi-view information
- We improve the training stability using a novel augmentation and conditioning scheme
- We make all code available at <https://github.com/m-kruse98/Multi-Flow>

2. Related Work

We review the field of anomaly detection and also give an overview of the research on normalizing flows.

2.1. Anomaly detection

Research on anomaly detection (AD) has differentiated into a number of varying types of algorithms. Fundamentally, most algorithms are semi-supervised, as they only learn using normal, anomaly-free, data.

One strand of research uses *reconstruction-based* methods. These usually aim to reconstruct images, or features, through some information bottleneck, with the underlying assumption that anomalies will not be as easily reconstructed. Early works used autoencoders [6, 67] or generative adversarial networks [1, 36, 52, 62]. These models are

especially prone to over-generalization, which may result in successful reconstruction for all types of inputs, contradicting the underlying assumptions of these methods.

Other methods have delved into *incorporating anomalous samples* into the training process, sitting between semi-supervised and fully supervised approaches. They may use actual real-world anomaly samples [43] or self-generated and simulated anomalous data [3, 34, 38, 61, 65] to fine-tune their decision boundaries. However, these methods need to be mindful of any biases they introduce towards their generated data.

Student-teacher networks have also seen a lot of usage in anomaly detection [4, 13, 51, 64]. In most of these, a student network is trained to mimic the behavior of a teacher network. Since training is done on normal data, the student usually fails to mimic the teacher on anomalous data, thereby enabling the detection. Designing suitable tasks for the teacher is very important for these networks.

With the de-facto standard data set MVTec AD [5] having reached near saturation in performance [38, 48], the research community has been looking for extensions to the current state-of-the-art. Some authors try to fit the detection of all classes in the data sets into one single model, a task termed *multi-class anomaly detection* [40, 58, 66]. Other works focus on *more difficult data sets*. These may need algorithms to perform logical reasoning [7] or work with other data modalities, such as 3D data, to detect anomalies [8, 9, 35, 37]. Other trends include detecting anomalies in *multi-view data*. Here, anomalies need to be detected in all views they appear in, irrespective of the object pose, making the task more difficult. Pose-agnostic anomaly detection, as posed in the MAD data set [68, 69], requires reasoning across dozens of views of one single object. While embedding this data into the 3D space using novel-view synthesis methods has seen some success, conventional 2D methods still struggle heavily in this setting [31, 68]. Another setting has been proposed with the Real-IAD data set [54], which, inspired by real production scenarios and factory camera setups, features five fixed camera poses per object. Contrary to MAD, which contains dozens of images of one specific normal instance [68, 69], Real-IAD contains much sparser multi-view data of many different normal instances [54]. Hence, Real-IAD requires reasoning across a huge range of multi-view instances, including their variation in texture and shape.

With the advent of large pre-trained foundation models for both image and text, a new branch surrounding few-shot or *zero-shot anomaly detection* methods has formed [20, 25, 70]. AnomalyGPT [20] leverages existing feature-based methods and contextualizes and verbalizes the found anomalies using a Large Language Model (LLM). Works such as WinCLIP [25] leverage the shared image-text latent space of CLIP embeddings [45] to detect anomalous con-

cepts without any training. While there is progress on the standard detection tasks, there is still work to be done in adapting the zero-shot methods to detect anomalies in data modalities other than regular single-view images.

Lastly, *density estimation* techniques have seen success in anomaly detection. These works leverage pre-trained features as their latent space on which they estimate a samples likelihood. This may be done with parametric models such as a multivariate Gaussian [12] or implicitly using nearest-neighbor methods [11, 32, 48]. These methods are highly dependent on the choice of features, as they require distances in feature space to correspond to the difference between anomalies and normal samples [22].

2.2. Normalizing Flows

Normalizing Flows are a widely applied set of techniques for anomaly detection [10, 21, 33, 47, 49, 50, 59], falling into the category of density estimation. These flows are invertible mappings between two distribution spaces. During the forward direction, this enables the expression of likelihoods within a complex feature distribution by means of a simpler base distribution, such as a standard Gaussian [46]. Due to the bijectivity of a flow, they can also be used in their backwards direction. It is possible to generate a sample from the base distribution and use the reverse direction of the flow. This generates a sample in the original complex distribution, giving the flow generative capabilities when training on e.g. images of human faces [28]. Nowadays, normalizing flows have fallen out of favor in many generative tasks, as diffusion models managed to achieve strong generation performances [24].

Still, normalizing flows fulfill an interesting niche when used for exact probability distribution modeling [49, 55, 57] or for problems bijective in nature [56]. A lot of research has also gone into proposing efficient neural network architectures, while preserving invertibility, among other criteria, for normalizing flows. Architectures using coupling blocks have seen wide application [15, 28], with RealNVP [16] being used for its simplicity and efficient computation. These methods partition the data and let these splits transform each other using learned (affine) transformations, all while preserving invertibility. Research has focused on proposing new expressive transformations such as ones based on rational quadratic splines [18] or other non-linear functions [23]. Lastly, normalizing flows can also be used in an autoregressive fashion [19, 29, 44]. While these autoregressive methods enjoy strong performances in some tasks, they have higher computational demands than RealNVP-based architectures. RealNVP only needs one forward pass for an estimate in either direction, whereas autoregressive models need to update their internal state, requiring several passes to compute the likelihood of a sample. Depending on their architecture, either sampling [44]

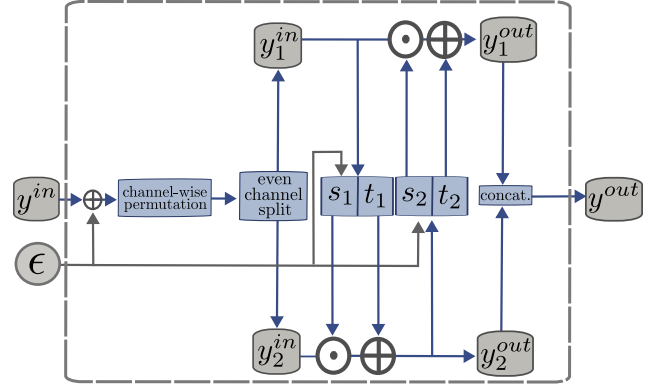


Figure 2. RealNVP [16] coupling block with conditioning. The input y^{in} is augmented with a noise vector ϵ and split into two parts along its channel dimension. Each split and the conditioning noise component ϵ is concatenated and given to an st -network, which calculates components s and t for transforming the opposing path.

or likelihood estimation [29] become more costly than their RealNVP counterpart.

3. Methodology

We describe the full training and testing procedure for our approach. It has been shown, that normalizing flows underperform in anomaly detection tasks, when training on raw image data [30]. We therefore learn our normalizing flow on a feature distribution $y \in \mathcal{Y}$, where we obtain each feature y using a standard pre-trained feature extractor f_F on input images $x \in \mathcal{X}$. Our normalizing flow, parametrized using a neural network, then maps these features onto the Gaussian distribution $p_{\mathcal{Z}}$. Therefore, we use the mappings

$$x \in \mathcal{X} \xrightarrow{f_F} y \in \mathcal{Y} \xleftrightarrow{f_\theta} z \in \mathcal{Z} \sim \mathcal{N}(0, I), \quad (1)$$

where f_F is the frozen feature extractor, and f_θ is our trainable bijective normalizing flow.

3.1. Model Setup

An image x_i is passed through a pre-trained feature extractor to receive a feature vector $y_i \in \mathbb{R}^{C \times W \times H}$. This vector serves as input to the flow model, which consists of several coupling blocks chained behind one another. A diagram of the information flow in such a coupling block can be found in Fig. 2. It consists of permuting and splitting along the channel dimension, and calculating the affine transformation as

$$\begin{aligned} y_1^{out} &= y_1^{in} \odot e^{s_2(y_2^{out})} \oplus t_2(y_2^{out}), \text{ and} \\ y_2^{out} &= y_2^{in} \odot e^{s_1(y_1^{in})} \oplus t_1(y_1^{in}). \end{aligned} \quad (2)$$

Here, \oplus and \odot are element-wise addition and multiplication, respectively. The most integral part are the

st -networks, which estimate additive and multiplicative element-wise components of the affine transformations. They will be described in greater detail in Sec. 3.3. To invert the entire model, additive components need to be subtracted, and multiplicative ones are divided.

We further apply a soft clamping to the scale coefficients s to increase the training stability [2] by constraining them to the interval of $[-\alpha, \alpha]$ using

$$s_{\text{clamp}} = \frac{2\alpha}{\pi} \arctan\left(\frac{s}{\alpha}\right). \quad (3)$$

Given a feature vector y our model puts out a pixel-wise likelihood estimate z , which also serves as the models anomaly score. Taking the maximum aggregates them into a single image-wise score. Further, the maximum operator is also used when aggregating scores of several multi-view images into one sample-wise score.

3.2. Background Removal

Currently, the model has to focus on the entire image feature space, including both foreground and background. Any irregularities, such as background dust or other particles, may also be detected as an anomaly, despite not constituting an actual product-related defect. Ignoring the background has been shown to improve detection results [51]. Therefore, we employ the state-of-the-art dichotomous image-segmentation network MVANet [60] to remove all background from foreground objects, as seen in Fig. 3. Here, we take the output of MVANet and apply a binary hole closing as well as an 8×8 dilation, to ensure getting one single-component to mask the entire object. We resize the masks to the same size as the extracted feature maps for use in training. By only calculating the loss on the foreground objects, we only estimate the object likelihood, ignoring the background completely. Thereby, the network can fully focus on estimating the objects likelihood and will not be distracted by confounding factors in the background.

3.3. Multi-View st -Network Design

The way the invertible RealNVP coupling blocks are designed, as seen in Fig. 2, networks s and t may be arbitrarily complex non-invertible neural networks. Since all the computational power of the normalizing flow resides in the st -network, we need to carefully choose their design.

With our model focusing on detecting the anomalies in a sample-wise fashion, we group the input to our model into batches of images belonging to the same instance. The model receives batches of n_v feature maps $\{y^i\}_{i=0}^{n_v}$ per instance, where each feature vector y^i corresponds to the image of the i -th camera. As for the case of Real-IAD, we therefore group together $n_v = 5$ different views. This allows for reasoning across views, which regular anomaly detection methods do not take into consideration. An overview of the paths of information flow is given in Fig. 4.



Figure 3. Examples of the background removal using the pre-trained dichotomous segmentation network MVANet [60] on Real-IAD [54]. The usually homogeneous background regions can be extracted in all cases and without any grave mistakes.

Each of the input vectors y^i get passed through a convolutional block, which transforms them into a new representation \hat{y}^i . This simple convolutional block consists of a two-dimensional convolution with 5×5 kernels in the last coupling layer and 3×3 kernels in all preceding ones, as well as a standard ReLU nonlinearity. The transformed vectors \hat{y}^i then serve as input to all further connecting paths in the st -network. Here, we aim to let information flow between neighboring views. This enables anomalous features that are easy to see in one view, to influence others, where they may be much harder to find. Still, we want to retain the models ability to also output separate anomaly maps for all input vectors, to enable the image-wise anomaly detection.

The most basic building block of all cross-view operations are 2D convolutions, denoted by f_{cross} . Each representation \hat{y}^i is enriched by information derived from all neighboring views. Thus, each feature map gets infused with multi-view information by calculating

$$y_{\text{output}}^i = f_{\text{cross}}^{ii}(\hat{y}^i) + \frac{1}{|N(\hat{y}^i)|} \sum_{j \in N(\hat{y}^i)} f_{\text{cross}}^{ji}(\hat{y}^j), \quad (4)$$

where $N(\hat{y}^i)$ denotes the set of all neighboring views of \hat{y}^i and f_{cross}^{ji} is the convolutional layer connecting the j -th view to the i -th view. We also consider every view \hat{y}^i as connected to itself, to further stabilize the image-wise likelihood estimation. While we define the exact camera neighbors for Real-IAD, this framework may be extended to other multi-view settings.

Top-View Connections. In Real-IAD, all objects contain one birds-eye view, and four surrounding views [54]. As visualized in Fig. 4, we consider the top-view a neighbor to all other surrounding views, letting information flow to all

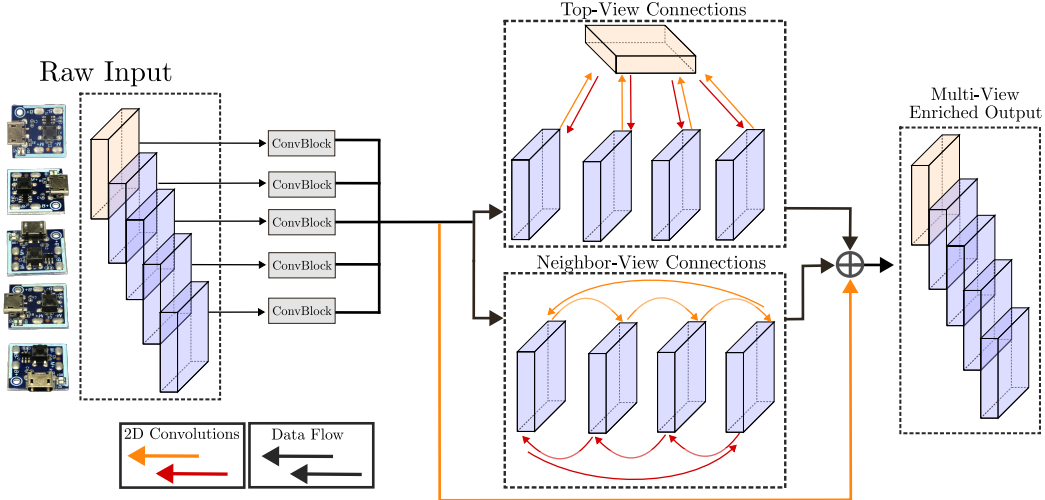


Figure 4. Architecture for sharing information across views. Each *st*-network implements one of these blocks. The raw input consists of a feature map for each of the object views. Each feature is finetuned by being passed through a ConvBlock. Then, subsequent 2D convolutions are applied and the data is aggregated according to the multi-view setup in Eq. (4). Top-view connections let information flow from the birds-eye view to all others. Neighbor-view connections lets the information flow between adjacent side views of the object.

side-views and vice-versa. In Fig. 4, each of the colored arrows here again denote a 2D convolution f_{cross} , which may represent the features according to the target-views needs.

Neighbor-View Connections. Continuing with letting information flow between adjacent views, we also consider all surrounding views next to each other to be neighbors. Again, each side-view passes and receives its information from the adjacent views on both the right and the left side. While it may be possible that opposing views also see similar object contents, we do not force any connections between them. Their relationships may instead be captured within the top-view connections of the architecture.

3.4. Training Objective

We want to maximize the likelihood of the training features $y \in \mathcal{Y}$. This is done by transforming them into the Gaussian space \mathcal{Z} , where measurements of likelihood $p_{\mathcal{Z}}(z)$ are easily tractable. When $f_{\theta}(y) = z$ is the output of our flow, we may express the feature distribution $p_{\mathcal{Y}}(y)$ using the *change-of-variables formula* as

$$p_{\mathcal{Y}}(y) = p_{\mathcal{Z}}(z) \left| \det \frac{\partial z}{\partial y} \right|. \quad (5)$$

Work such as SimpleNet [38] add noise to the training samples, to better approximate the entire feature space, including anomalous features, while avoiding overfitting. Following SoftFlow [27], we sample noise ϵ during training and use them as additive components to perturb the training data points as

$$x' = x + \epsilon, \text{ where } \epsilon \sim \mathcal{N}(0, c^2 I). \quad (6)$$

SimpleNet [38] makes use of this noise to generate pseudo-anomalies to train a discriminator. We do not explicitly model a discriminator but rather use this noise as a condition for the normalizing flow, letting it learn the conditional mapping $f_{\theta}(y|\epsilon) = z$. This lets the flow more easily approximate the entire data manifold of both normal and anomalous samples [27]. Since $p_{\mathcal{Z}}(z)$ is parametrized as a standard normal gaussian, maximum likelihood training using Eq. (5) simplifies to the loss function

$$\mathcal{L}(y) = -\log p_{\mathcal{Y}}(y) = \frac{\|z\|_2^2}{2} - \left| \det \frac{\partial z}{\partial y} \right|, \quad (7)$$

where $z = f_{\theta}(y|\epsilon)$.

This is also the formula to calculate the anomaly maps with their respective anomaly scores, resulting in high values (i.e. low likelihood) for anomalous regions, and low values (i.e. high likelihoods) for normal regions. With the architecture from RealNVP, the determinant of the Jacobian $\frac{\partial z}{\partial y}$ in Eq. (7) reduces to the sum of all scale values s in the coupling blocks.

4. Experiments

We evaluate our approach both quantitatively and qualitatively and compare it to several state-of-the-art methods.

4.1. Evaluation Setting

All models are trained in a semi-supervised fashion, i.e. all training examples are known to be defect-free. Furthermore, the model knows the camera-to-object grouping, enabling it to reason about an object across views. Validation is done on the standard test set, containing both

Metrics	PaDiM	Cflow	SoftPatch	DeSTSeg	RD	UniAD	PatchCore	SimpleNet	<i>Multi-Flow</i>
AUROC (\uparrow)	[12]	[21]	[26]	[64]	[13]	[58]	[48]	[38]	(ours)
Sample-wise	91.2	89.8	92.8	94.0	83.7	88.1	93.7	94.9	95.85 \pm 0.02
Image-wise	80.3	82.5	<u>89.4</u>	86.9	87.1	82.9	<u>89.4</u>	88.5	90.27 \pm 0.02

Table 1. **Average** detection performance of various methods across all classes in Real-IAD [54]. Sample-wise denotes the setting, where the score of images of the same object are aggregated to one single score. Image-wise treats every image as an independent instance. Best performances are **bold**, with the runner-up underlined. We execute our method for $n = 5$ runs and report mean \pm standard deviation.

normal and large amounts of anomalous samples. We train one model per object class, and compare to a wide range of state-of-the-art algorithms, similarly trained in a semi-supervised and one-model-per-class fashion. Comparisons are done to baseline models PaDiM [12], Cflow [21], SoftPatch [26], DeSTSeg [64], Reverse-Distillation [13], UniAD [58], PatchCore [48] and SimpleNet [38], whose numbers are taken from the original Real-IAD paper [54]. These provide a good range across both older and recent state-of-the-art methods as well as a mix of different paradigms, such as density estimation or student-teacher networks.

4.2. Dataset and Metrics

Real-IAD [54] is a large anomaly detection data set, comprised of 30 different object classes, with roughly 3000 defect-free and 1700 anomalous images per class. This is magnitudes larger than previous data sets [5, 42, 71]. Each object instance contains views from the object sides (i.e. 4 side-views) and one top-view from the bird perspective. Anomalies are grouped into one of eight categories, such as deformations, scratches, missing parts, or foreign objects.

We follow the standard procedures, as proposed by the respective data sets, for evaluation [5, 54]. The detection may either be measured *image-wise* (i.e. each image is treated as an independent instance), or *sample-wise* (multi-view images of the same object instance are aggregated into one sample). Both are measured using the Area Under the Receiver Operating Curve (AUROC), which measures detection performance independent of any thresholds. Segmenting the anomalous regions will be evaluated by calculating the AUROC for each pixel, and the AUPRO [5], which is more sophisticated at measuring performance irrespective of the size of anomaly.

4.3. Implementation Details

We resize all images to a size of 768×768 pixels, and pass them through the extractor f_F , which is implemented by an EfficientNet-b5 [53] pre-trained on the general purpose ImageNet data set [14]. Similar to other methods [50, 51] we extract the intermediate features after the 36-th layer, resulting in 304 feature maps of size 24×24 pixels, which suffices for a good anomaly segmentation performance. We chain together six coupling blocks for our architecture, with

the scale factors clamped using $\alpha = 1.9$ in Eq. (3).

Training and optimization is done for 112 epochs using the AdamW optimizer [39] with a learning rate of $2 \cdot 10^{-4}$, a weight decay of 10^{-5} , and momentum parameters $\beta_1 = 0.9$ and $\beta_2 = 0.95$. The ConvBlocks in the *st*-networks work with a hidden feature dimension of 64, which is brought back up by the later convolutional connections. The noise ϵ is sampled with a fixed $c^2 = 0.15$. We follow the data loading implementation from Real-IAD [54], leaving out any augmentations that may alter the contents of the images. Evaluation is done with the efficient and GPU-accelerated computation methods provided by ADEval [63].

4.4. Anomaly Detection Results

The main results for the image and sample-wise anomaly detection, averaged across all classes of Real-IAD, can be found in Tab. 1. More comprehensive results for each of the single classes are in the appendix in Tab. 5 and Tab. 6.

As visible in Tab. 1, we are able to outperform all baselines in the detection tasks. In the sample-wise prediction task, where we aggregate the anomaly scores across views, we reach a new state-of-the-art with an AUROC of 95.85. This is an improvement over the current best-performing model SimpleNet, which sits at a sample-wise AUROC of 94.9. As for the image-wise detection, where each image is treated as an i.i.d. sample, we also slightly outperform all baselines with an AUROC of 90.27, while the next best competitors SoftPatch and PatchCore both reach 89.4.

Since pixel-precise and accurate segmentation is not the focus of our method, we slightly lack behind in the segmentation metrics, as we achieve a pixel-wise AUROC of 96.47 and an AUPRO of 87.91, while the best competitor RD achieves and AUPRO of 93.8. The full results of the segmentation task can be found in the appendix in Tab. 7. Future work could deal with improving the segmentation capabilities of normalizing flow-based anomaly detection methods, which have been known to be improvable, despite their very strong detection performance [49, 50].

We also provide qualitative results for four different objects, seen from all five viewpoints, in Fig. 5. Here, we can observe that anomalies are being detected in all of the different views of the camera setup, irrespective of their location. Furthermore, when anomalies are only present in some of the views, their errors do not wrongly carry over to

views without anomalies. This enables our approach to also perform well in the image-wise setting, where each view is treated independently.

4.5. Ablation Studies

We conduct ablation studies on our design choices, including cross-view connections, the background removal, the fusion functions f_{cross} , and the noise conditioning.

4.5.1. Impact of Cross-View Connections

We conduct an ablation study on the effectiveness of the cross-view connections introduced in Sec. 3.3 and visualized in Fig. 4. We remove the connections to neighboring and/or to the top-view and re-run our experiments. The result of this ablation can be found in Tab. 2. Here, it becomes apparent that removing all cross-view connections leads to a worse sample-wise detection performance. Further, including any of our proposed cross-view connection blocks improves the sample-wise detection substantially, while slightly deteriorating the image-wise score. Lastly, the combination of both types of connections, top-view and neighboring-view, leads to the best performance in both metrics, which further motivates our choice of cross-view connections and architecture.

Connection Type		AUROC (\uparrow)	
Top-View	Neighboring	Sample-wise	Image-wise
×	×	94.62	<u>90.25</u>
✓	×	95.50	90.03
×	✓	<u>95.61</u>	90.19
✓	✓	95.85	90.27

Table 2. Ablation on different cross-view neighborhood choices. Best performances are **bold**, with the runner-up underlined.

4.5.2. Impact of Background Removal

Removing the background and calculating the loss only on the foreground object greatly boosts the detection performance. The image-wise detection is boosted from an AUROC of 85.00 across all classes in Real-IAD to an AUROC of 90.27, which is a 6.2% boost in performance. This may be attributed to the model focusing more clearly on the object. Further, it is no longer confused by dust particles or other irritating background factors. This makes background removal a crucial feature for precise detection performance.

However, it does come at a cost, as the segmentation performance, measured by the Pixel-AUROC metric, drops from 97.29 to 96.47 when removing the background information, while AUPRO stays roughly the same. We argue, that while the masks provided by the MVANet are very precise, they do end up pruning some of the relevant information. The pixels in the extracted feature space all contain information tied to a larger receptive field. This may in turn

result in removed feature pixels to still contain some valuable information about the object, to which the model does not have access anymore. Furthermore, masking of anomalous regions, such as missing parts, is introduced as a new, albeit rare, source of error. Nevertheless, we still suggest to use the background removal, as it guides the model to focus on the important parts of the feature distribution. Any successes in detection or segmentation that may be attributed to uncontrollable background factors are eliminated after all.

4.6. Impact of Feature-Fusion Architecture

We further test the capabilities of other information fusion techniques for our cross-view connections.

f_{cross}	← AUROC (\uparrow) →			
	AUPRO	Pixel	Sample	Image
Self-Attention	87.94	96.48	95.19	89.63
Cross-View Att.	88.17	96.54	<u>95.27</u>	89.95
2D Convolution	87.91	96.47	95.85	90.27

Table 3. Comparison of different multi-view feature fusion methods for the cross-view connections f_{cross} . Best performances are **bold**, with the runner-up underlined.

All the cross-view connections f_{cross} discussed in Sec. 3.3 and Fig. 4 consist of a 2D convolutional layer to finetune the neighboring features. Here, the convolution is applied to the neighboring view, and summed up together with the original source view, as stated in Eq. (4). This mechanism is most easily replaced by an attention mechanism applied to the neighboring view, which is the main building block of the popular vision transformers [17]. For self-attention, instead of a single 2D convolution, we apply a multi-head self-attention layer, layer normalization, and ReLU activation to the neighboring view before summation. Adding to that, for cross-view attention, we use the source view \hat{y}^i as query and key to the attention mechanism, and the neighboring views $\hat{y}^j \in N(\hat{y}^i)$ as the value, while keeping the rest of the block the same.

As visible in Tab. 3, cross-view attention beats out self-attention in all metrics. However, the simplicity and fast convergence of the 2D convolutions out-performs both attention mechanisms in the detection tasks, while being slightly inferior in the segmentation metrics. Since attention layers greatly increase both memory requirements and inference speed, we prefer to use the convolutional blocks for deployment in real-life scenarios. However, for larger data sets, switching to attention may yield more benefit and could be part of future research endeavors [41].

4.7. Impact of Augmentation & Conditioning

We study the impact of using the different noise schemes for augmenting the data and conditioning our normalizing flow. The results for anomaly detection can be found in Tab. 4.

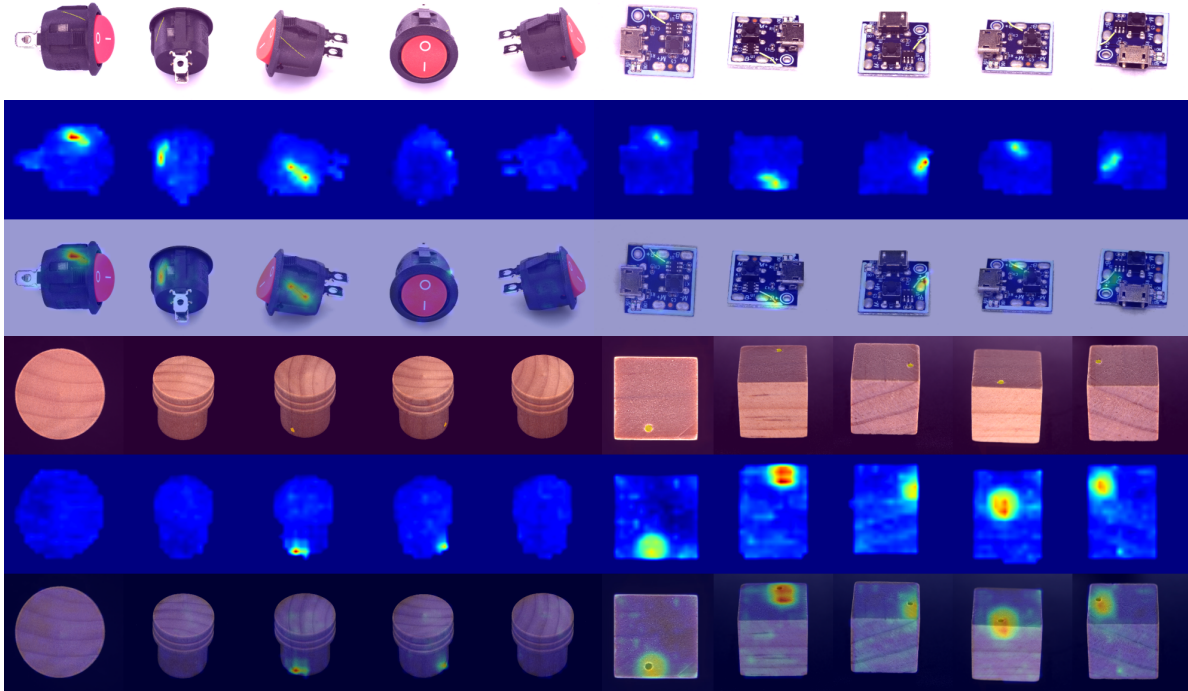


Figure 5. Qualitative results of detecting anomalies in various multi-view poses. For each object, the top row contains the image with anomalies marked. The middle row is the raw anomaly map output by the model. The lower row contains a superimposition of both input image and anomaly map values. The depicted classes are "Switch", "PCB", "Fire Hood", and "Toy Brick".

Multi-Flow samples noise similar to SimpleNet [38], with vectors $\epsilon \sim \mathcal{N}(0, 0.15 \cdot I)$ which are added to the input features, to regularize training. We also test sampling noise uniformly as $\epsilon \sim U(0, 1)$. Similar to SoftFlow [27], which originally proposed conditioning normalizing flows with noise, we also test their sampling strategy. It involves drawing a vector $c \sim U(0, 1)$ and then sampling noise as $\epsilon \sim \mathcal{N}(0, c^2 \cdot I)$. Compared to SimpleNet, this results in more variance in the noise distribution.

As visible in Tab. 4, the different noise conditioning schemes only slightly influence the segmentation metrics AUPRO and Pixel-AUROC. As for the detection tasks, which is our focus, there are slight advantages for both the SoftFlow and SimpleNet schemes for the image and sample-wise AUROC respectively. In the end, we propose to use the conditioning scheme proposed by SimpleNet, resulting in a slightly boosted sample-wise performance, as well as a relatively strong performance in all other metrics.

5. Conclusion

In this paper, we proposed a novel normalizing flow-based architecture to perform anomaly detection in multi-view image data. We have designed a new architecture and training scheme tailored to multi-view setups. This allows the flow to share its information across views, boosting the perfor-

Noise-type	AUPRO	← AUROC (↑) →		
		Pixel	Sample	Image
No Noise	87.92	96.47	95.84	90.25
Uniform	87.67	96.38	95.54	90.23
SoftFlow [27]	87.89	96.47	95.77	90.41
SimpleNet [38]	<u>87.91</u>	96.47	95.85	<u>90.27</u>

Table 4. Comparison on the noise conditioning, with *Multi-Flow* using the SimpleNet-esque method. Best performances are **bold**, with the runner-up underlined.

mance in both image and sample-wise anomaly detection.

Future work could look towards extending to data sets with less rigid camera setups, where dozens of views of an object may be available [31, 69]. Encoding similar architectural priors into other tasks, such as logical anomaly detection [7], may be another interesting future avenue.

Acknowledgements. This work was supported by the Federal Ministry of Education and Research (BMBF), Germany, under the AI service center KISSKI (grant no. 01IS22093C), the MWK of Lower Saxony within Hybrint (VWZN4219), the Deutsche Forschungsgemeinschaft (DFG) under Germany’s Excellence Strategy within the Cluster of Excellence PhoenixD (EXC2122), the European Union under grant agreement no. 101136006 – XTREME.

References

- [1] Samet Akcay, Amir Atapour-Abarghouei, and Toby P Breckon. Ganomaly: Semi-supervised anomaly detection via adversarial training. In *Computer Vision–ACCV 2018: 14th Asian Conference on Computer Vision, Perth, Australia, December 2–6, 2018, Revised Selected Papers, Part III 14*, pages 622–637. Springer, 2019. 2
- [2] Lynton Ardizzone, Carsten T. Lüth, Jakob Kruse, Carsten Rother, and Ullrich Köthe. Guided image generation with conditional invertible neural networks. *CoRR*, abs/1907.02392, 2019. 4
- [3] Jaehyeok Bae, Jae-Han Lee, and Seyun Kim. PNI: industrial anomaly detection using position and neighborhood information. In *IEEE/CVF International Conference on Computer Vision, ICCV 2023, Paris, France, October 1-6, 2023*, pages 6350–6360. IEEE, 2023. 2
- [4] Kilian Batzner, Lars Heckler, and Rebecca König. Efficiantad: Accurate visual anomaly detection at millisecond-level latencies. In *Proceedings of the IEEE/CVF Winter Conference on Applications of Computer Vision (WACV)*, pages 128–138, 2024. 2
- [5] Paul Bergmann, Michael Fauser, David Sattlegger, and Carsten Steger. Mvtec ad—a comprehensive real-world dataset for unsupervised anomaly detection. In *Proceedings of the IEEE/CVF conference on computer vision and pattern recognition*, pages 9592–9600, 2019. 1, 2, 6
- [6] Paul Bergmann, Sindy Löwe, Michael Fauser, David Sattlegger, and Carsten Steger. Improving unsupervised defect segmentation by applying structural similarity to autoencoders. In *Proceedings of the 14th International Joint Conference on Computer Vision, Imaging and Computer Graphics Theory and Applications, VISIGRAPP 2019, Volume 5: VISAPP, Prague, Czech Republic, February 25-27, 2019*, pages 372–380, 2019. 2
- [7] Paul Bergmann, Kilian Batzner, Michael Fauser, David Sattlegger, and Carsten Steger. Beyond dents and scratches: Logical constraints in unsupervised anomaly detection and localization. *International Journal of Computer Vision*, 130(4):947–969, 2022. 1, 2, 8
- [8] Paul Bergmann, Xin Jin, David Sattlegger, and Carsten Steger. The mvtec 3d-ad dataset for unsupervised 3d anomaly detection and localization. In *Proceedings of the 17th International Joint Conference on Computer Vision, Imaging and Computer Graphics Theory and Applications, VISIGRAPP 2022, Volume 5: VISAPP, Online Streaming, February 6-8, 2022*, pages 202–213. SCITEPRESS, 2022. 2
- [9] Luca Bonfiglioli, Marco Toschi, Davide Silvestri, Nicola Fioraio, and Daniele De Gregorio. The eyecandies dataset for unsupervised multimodal anomaly detection and localization. In *Proceedings of the Asian Conference on Computer Vision*, pages 3586–3602, 2022. 2
- [10] Jan Thieß Brockmann, Marco Rudolph, Bodo Rosenhahn, and Bastian Wandt. The voraus-ad dataset for anomaly detection in robot applications. *IEEE Trans. Robotics*, 40:438–451, 2024. 3
- [11] Niv Cohen and Yedid Hoshen. Sub-image anomaly detection with deep pyramid correspondences. *arXiv preprint arXiv:2005.02357*, 2020. 3
- [12] Thomas Defard, Aleksandr Setkov, Angélique Loesch, and Romaric Audigier. Padim: a patch distribution modeling framework for anomaly detection and localization. In *International Conference on Pattern Recognition*, pages 475–489. Springer, 2021. 3, 6, 1, 2
- [13] Hanqiu Deng and Xingyu Li. Anomaly detection via reverse distillation from one-class embedding. In *Proceedings of the IEEE/CVF Conference on Computer Vision and Pattern Recognition*, pages 9737–9746, 2022. 2, 6, 1
- [14] Jia Deng, Wei Dong, Richard Socher, Li-Jia Li, Kai Li, and Li Fei-Fei. Imagenet: A large-scale hierarchical image database. In *2009 IEEE conference on computer vision and pattern recognition*, pages 248–255. Ieee, 2009. 6
- [15] Laurent Dinh, David Krueger, and Yoshua Bengio. NICE: non-linear independent components estimation. In *3rd International Conference on Learning Representations, ICLR 2015, San Diego, CA, USA, May 7-9, 2015, Workshop Track Proceedings*, 2015. 3
- [16] Laurent Dinh, Jascha Sohl-Dickstein, and Samy Bengio. Density estimation using real NVP. In *5th International Conference on Learning Representations, ICLR 2017, Toulon, France, April 24-26, 2017, Conference Track Proceedings*. OpenReview.net, 2017. 3
- [17] Alexey Dosovitskiy, Lucas Beyer, Alexander Kolesnikov, Dirk Weissenborn, Xiaohua Zhai, Thomas Unterthiner, Mostafa Dehghani, Matthias Minderer, Georg Heigold, Sylvain Gelly, Jakob Uszkoreit, and Neil Houlsby. An image is worth 16x16 words: Transformers for image recognition at scale. In *9th International Conference on Learning Representations, ICLR 2021, Virtual Event, Austria, May 3-7, 2021*. OpenReview.net, 2021. 7
- [18] Conor Durkan, Artur Bekasov, Iain Murray, and George Papamakarios. Neural spline flows. In *Advances in Neural Information Processing Systems 32: Annual Conference on Neural Information Processing Systems 2019, NeurIPS 2019, December 8-14, 2019, Vancouver, BC, Canada*, pages 7509–7520, 2019. 3
- [19] Mathieu Germain, Karol Gregor, Iain Murray, and Hugo Larochelle. MADE: masked autoencoder for distribution estimation. In *Proceedings of the 32nd International Conference on Machine Learning, ICML 2015, Lille, France, 6-11 July 2015*, pages 881–889. JMLR.org, 2015. 3
- [20] Zhaopeng Gu, Bingke Zhu, Guibo Zhu, Yingying Chen, Ming Tang, and Jinqiao Wang. Anomalygpt: Detecting industrial anomalies using large vision-language models. In *Thirty-Eighth AAAI Conference on Artificial Intelligence, AAAI 2024*, pages 1932–1940. AAAI Press, 2024. 2
- [21] Denis Gudovskiy, Shun Ishizaka, and Kazuki Kozuka. Cflow-ad: Real-time unsupervised anomaly detection with localization via conditional normalizing flows. In *Proceedings of the IEEE/CVF Winter Conference on Applications of Computer Vision*, pages 98–107, 2022. 3, 6, 1, 2
- [22] Lars Heckler, Rebecca König, and Paul Bergmann. Exploring the importance of pretrained feature extractors for unsupervised anomaly detection and localization. In *IEEE/CVF*

- Conference on Computer Vision and Pattern Recognition, CVPR 2023 - Workshops, Vancouver, BC, Canada, June 17-24, 2023*, pages 2917–2926. IEEE, 2023. 3
- [23] Jonathan Ho, Xi Chen, Aravind Srinivas, Yan Duan, and Pieter Abbeel. Flow++: Improving flow-based generative models with variational dequantization and architecture design. In *Proceedings of the 36th International Conference on Machine Learning, ICML 2019, 9-15 June 2019, Long Beach, California, USA*, pages 2722–2730. PMLR, 2019. 3
- [24] Jonathan Ho, Ajay Jain, and Pieter Abbeel. Denoising diffusion probabilistic models. In *Advances in Neural Information Processing Systems 33: Annual Conference on Neural Information Processing Systems 2020, NeurIPS 2020, December 6-12, 2020, virtual*, 2020. 3
- [25] Jongheon Jeong, Yang Zou, Taewan Kim, Dongqing Zhang, Avinash Ravichandran, and Onkar Dabeer. Winclip: Zero/few-shot anomaly classification and segmentation. In *IEEE/CVF Conference on Computer Vision and Pattern Recognition, CVPR 2023, Vancouver, BC, Canada, June 17-24, 2023*, pages 19606–19616. IEEE, 2023. 2
- [26] Xi Jiang, Jianlin Liu, Jinbao Wang, Qiang Nie, Kai Wu, Yong Liu, Chengjie Wang, and Feng Zheng. Softpatch: Unsupervised anomaly detection with noisy data. *Advances in Neural Information Processing Systems*, 35:15433–15445, 2022. 6, 1, 2
- [27] Hyeongju Kim, Hyeonseung Lee, Woo Hyun Kang, Joun Yeop Lee, and Nam Soo Kim. Softflow: Probabilistic framework for normalizing flow on manifolds. In *Advances in Neural Information Processing Systems 33: Annual Conference on Neural Information Processing Systems 2020, NeurIPS 2020, December 6-12, 2020, virtual*, 2020. 5, 8
- [28] Diederik P. Kingma and Prafulla Dhariwal. Glow: Generative flow with invertible 1x1 convolutions. In *Advances in Neural Information Processing Systems 31: Annual Conference on Neural Information Processing Systems 2018, NeurIPS 2018, December 3-8, 2018, Montréal, Canada*, pages 10236–10245, 2018. 2, 3
- [29] Diederik P. Kingma, Tim Salimans, Rafal Józefowicz, Xi Chen, Ilya Sutskever, and Max Welling. Improving variational autoencoders with inverse autoregressive flow. In *Advances in Neural Information Processing Systems 29: Annual Conference on Neural Information Processing Systems 2016, December 5-10, 2016, Barcelona, Spain*, pages 4736–4744, 2016. 3
- [30] Polina Kirichenko, Pavel Izmailov, and Andrew Gordon Wilson. Why normalizing flows fail to detect out-of-distribution data. In *Advances in Neural Information Processing Systems 33: Annual Conference on Neural Information Processing Systems 2020, NeurIPS 2020, December 6-12, 2020, virtual*, 2020. 3
- [31] Mathis Kruse, Marco Rudolph, Dominik Woiwode, and Bodo Rosenhahn. Splatpose & detect: Pose-agnostic 3d anomaly detection. In *IEEE/CVF Conference on Computer Vision and Pattern Recognition, CVPR 2024 - Workshops, Seattle, WA, USA, June 17-18, 2024*, pages 3950–3960. IEEE, 2024. 1, 2, 8
- [32] Sungwook Lee, Seunghyun Lee, and Byung Cheol Song. CFA: coupled-hypersphere-based feature adaptation for target-oriented anomaly localization. *IEEE Access*, 10: 78446–78454, 2022. 3
- [33] Jiarui Lei, Xiaobo Hu, Yue Wang, and Dong Liu. Pyramid-flow: High-resolution defect contrastive localization using pyramid normalizing flow. In *Proceedings of the IEEE/CVF Conference on Computer Vision and Pattern Recognition*, pages 14143–14152, 2023. 3
- [34] Chun-Liang Li, Kihyuk Sohn, Jinsung Yoon, and Tomas Pfister. Cutpaste: Self-supervised learning for anomaly detection and localization. In *Proceedings of the IEEE/CVF conference on computer vision and pattern recognition*, pages 9664–9674, 2021. 2
- [35] Wenqiao Li, Xiaohao Xu, Yao Gu, Bozhong Zheng, Shenghua Gao, and Yingna Wu. Towards scalable 3d anomaly detection and localization: A benchmark via 3d anomaly synthesis and A self-supervised learning network. In *IEEE/CVF Conference on Computer Vision and Pattern Recognition, CVPR 2024, Seattle, WA, USA, June 16-22, 2024*, pages 22207–22216. IEEE, 2024. 2
- [36] Yufei Liang, Jiangning Zhang, Shiwei Zhao, Runze Wu, Yong Liu, and Shuwen Pan. Omni-frequency channel-selection representations for unsupervised anomaly detection. *IEEE Transactions on Image Processing*, 2023. 2
- [37] Jiaqi Liu, Guoyang Xie, Ruitao Chen, Xinpeng Li, Jinbao Wang, Yong Liu, Chengjie Wang, and Feng Zheng. Real3d-ad: A dataset of point cloud anomaly detection. In *Advances in Neural Information Processing Systems 36: Annual Conference on Neural Information Processing Systems 2023, NeurIPS 2023, New Orleans, LA, USA, December 10 - 16, 2023*, 2023. 2
- [38] Zhikang Liu, Yiming Zhou, Yuansheng Xu, and Zilei Wang. Simplenet: A simple network for image anomaly detection and localization. In *Proceedings of the IEEE/CVF Conference on Computer Vision and Pattern Recognition*, pages 20402–20411, 2023. 1, 2, 5, 6, 8
- [39] Ilya Loshchilov and Frank Hutter. Decoupled weight decay regularization. In *7th International Conference on Learning Representations, ICLR 2019, New Orleans, LA, USA, May 6-9, 2019*. OpenReview.net, 2019. 6
- [40] Ruiying Lu, Yujie Wu, Long Tian, Dongsheng Wang, Bo Chen, Xiyang Liu, and Ruimin Hu. Hierarchical vector quantized transformer for multi-class unsupervised anomaly detection. In *Advances in Neural Information Processing Systems 36: Annual Conference on Neural Information Processing Systems 2023, NeurIPS 2023, New Orleans, LA, USA, December 10 - 16, 2023*, 2023. 2
- [41] Zhiying Lu, Hongtao Xie, Chuanbin Liu, and Yongdong Zhang. Bridging the gap between vision transformers and convolutional neural networks on small datasets. In *Advances in Neural Information Processing Systems 35: Annual Conference on Neural Information Processing Systems 2022, NeurIPS 2022, New Orleans, LA, USA, November 28 - December 9, 2022*, 2022. 7
- [42] Pankaj Mishra, Riccardo Verk, Daniele Fornasier, Claudio Piciarelli, and Gian Luca Foresti. Vt-adl: A vision trans-

- former network for image anomaly detection and localization. In *2021 IEEE 30th International Symposium on Industrial Electronics (ISIE)*, pages 01–06. IEEE, 2021. 6
- [43] Guansong Pang, Chunhua Shen, and Anton van den Hengel. Deep anomaly detection with deviation networks. In *Proceedings of the 25th ACM SIGKDD International Conference on Knowledge Discovery & Data Mining, KDD 2019, Anchorage, AK, USA, August 4-8, 2019*, pages 353–362. ACM, 2019. 2
- [44] George Papamakarios, Iain Murray, and Theo Pavlakou. Masked autoregressive flow for density estimation. In *Advances in Neural Information Processing Systems 30: Annual Conference on Neural Information Processing Systems 2017, December 4-9, 2017, Long Beach, CA, USA*, pages 2338–2347, 2017. 3
- [45] Alec Radford, Jong Wook Kim, Chris Hallacy, Aditya Ramesh, Gabriel Goh, Sandhini Agarwal, Girish Sastry, Amanda Askell, Pamela Mishkin, Jack Clark, Gretchen Krueger, and Ilya Sutskever. Learning transferable visual models from natural language supervision. In *Proceedings of the 38th International Conference on Machine Learning, ICML 2021, 18-24 July 2021, Virtual Event*, pages 8748–8763. PMLR, 2021. 2
- [46] Danilo Jimenez Rezende and Shakir Mohamed. Variational inference with normalizing flows. In *Proceedings of the 32nd International Conference on Machine Learning, ICML 2015, Lille, France, 6-11 July 2015*, pages 1530–1538. JMLR.org, 2015. 3
- [47] Bodo Rosenhahn and Christoph Hirche. Quantum normalizing flows for anomaly detection. *Physical Review A*, 110: 022443, 2024. 3
- [48] Karsten Roth, Latha Pemula, Joaquin Zepeda, Bernhard Schölkopf, Thomas Brox, and Peter Gehler. Towards total recall in industrial anomaly detection. In *Proceedings of the IEEE/CVF Conference on Computer Vision and Pattern Recognition*, pages 14318–14328, 2022. 1, 2, 3, 6
- [49] Marco Rudolph, Bastian Wandt, and Bodo Rosenhahn. Same same but different: Semi-supervised defect detection with normalizing flows. In *Proceedings of the IEEE/CVF winter conference on applications of computer vision*, pages 1907–1916, 2021. 2, 3, 6
- [50] Marco Rudolph, Tom Wehrbein, Bodo Rosenhahn, and Bastian Wandt. Fully convolutional cross-scale-flows for image-based defect detection. In *Proceedings of the IEEE/CVF Winter Conference on Applications of Computer Vision*, pages 1088–1097, 2022. 2, 3, 6
- [51] Marco Rudolph, Tom Wehrbein, Bodo Rosenhahn, and Bastian Wandt. Asymmetric student-teacher networks for industrial anomaly detection. In *WACV*, pages 2591–2601. IEEE, 2023. 2, 4, 6
- [52] Thomas Schlegl, Philipp Seeböck, Sebastian M Waldstein, Ursula Schmidt-Erfurth, and Georg Langs. Unsupervised anomaly detection with generative adversarial networks to guide marker discovery. In *International conference on information processing in medical imaging*, pages 146–157. Springer, 2017. 2
- [53] Mingxing Tan and Quoc V. Le. Efficientnet: Rethinking model scaling for convolutional neural networks. In *Proceedings of the 36th International Conference on Machine Learning, ICML 2019, 9-15 June 2019, Long Beach, California, USA*, pages 6105–6114. PMLR, 2019. 6
- [54] Chengjie Wang, Wenbing Zhu, Bin-Bin Gao, Zhenye Gan, Jiangning Zhang, Zhihao Gu, Shuguang Qian, Mingang Chen, and Lizhuang Ma. Real-iad: A real-world multi-view dataset for benchmarking versatile industrial anomaly detection. In *IEEE/CVF Conference on Computer Vision and Pattern Recognition, CVPR 2024, Seattle, WA, USA, June 16-22, 2024*, pages 22883–22892. IEEE, 2024. 1, 2, 4, 6
- [55] Xiaoyang Wang, Huihui Bai, Limin Yu, Yao Zhao, and Jimin Xiao. Towards the uncharted: Density-descending feature perturbation for semi-supervised semantic segmentation. In *IEEE/CVF Conference on Computer Vision and Pattern Recognition, CVPR 2024, Seattle, WA, USA, June 16-22, 2024*, pages 3303–3312. IEEE, 2024. 3
- [56] Tom Wehrbein, Marco Rudolph, Bodo Rosenhahn, and Bastian Wandt. Probabilistic monocular 3d human pose estimation with normalizing flows. In *2021 IEEE/CVF International Conference on Computer Vision, ICCV 2021, Montreal, QC, Canada, October 10-17, 2021*, pages 11179–11188. IEEE, 2021. 3
- [57] Tom Wehrbein, Marco Rudolph, Bodo Rosenhahn, and Bastian Wandt. Utilizing uncertainty in 2d pose detectors for probabilistic 3d human mesh recovery. In *Proceedings of the IEEE/CVF Winter Conference on Applications of Computer Vision*, 2025. 3
- [58] Zhiyuan You, Lei Cui, Yujun Shen, Kai Yang, Xin Lu, Yu Zheng, and Xinyi Le. A unified model for multi-class anomaly detection. *Advances in Neural Information Processing Systems*, 35:4571–4584, 2022. 2, 6, 1
- [59] Jiawei Yu, Ye Zheng, Xiang Wang, Wei Li, Yushuang Wu, Rui Zhao, and Liwei Wu. Fastflow: Unsupervised anomaly detection and localization via 2d normalizing flows. *arXiv preprint arXiv:2111.07677*, 2021. 3
- [60] Qian Yu, Xiaoqi Zhao, Youwei Pang, Lihe Zhang, and Huchuan Lu. Multi-view aggregation network for dichotomous image segmentation. In *Proceedings of the IEEE/CVF Conference on Computer Vision and Pattern Recognition (CVPR)*, pages 3921–3930, 2024. 4
- [61] Vitjan Zavrtanik, Matej Kristan, and Danijel Skočaj. Draem—a discriminatively trained reconstruction embedding for surface anomaly detection. In *Proceedings of the IEEE/CVF International Conference on Computer Vision*, pages 8330–8339, 2021. 2
- [62] Gongjie Zhang, Kaiwen Cui, Tzu-Yi Hung, and Shijian Lu. Defect-gan: High-fidelity defect synthesis for automated defect inspection. In *Proceedings of the IEEE/CVF Winter Conference on Applications of Computer Vision*, pages 2524–2534, 2021. 2
- [63] Jiangning Zhang, Haoyang He, Zhenye Gan, Qingdong He, Yuxuan Cai, Zhucun Xue, Yabiao Wang, Chengjie Wang, Lei Xie, and Yong Liu. Ader: A comprehensive benchmark for multi-class visual anomaly detection. *arXiv preprint arXiv:2406.03262*, 2024. 6
- [64] Xuan Zhang, Shiyu Li, Xi Li, Ping Huang, Jiulong Shan, and Ting Chen. Destseg: Segmentation guided denoising

- student-teacher for anomaly detection. In *Proceedings of the IEEE/CVF Conference on Computer Vision and Pattern Recognition*, pages 3914–3923, 2023. [2](#), [6](#), [1](#)
- [65] Ximiao Zhang, Min Xu, and Xiuzhuang Zhou. Realnet: A feature selection network with realistic synthetic anomaly for anomaly detection. In *IEEE/CVF Conference on Computer Vision and Pattern Recognition, CVPR 2024, Seattle, WA, USA, June 16-22, 2024*, pages 16699–16708. IEEE, 2024. [2](#)
- [66] Ying Zhao. Omnia: A unified CNN framework for unsupervised anomaly localization. In *IEEE/CVF Conference on Computer Vision and Pattern Recognition, CVPR 2023, Vancouver, BC, Canada, June 17-24, 2023*, pages 3924–3933. IEEE, 2023. [2](#)
- [67] Chong Zhou and Randy C Paffenroth. Anomaly detection with robust deep autoencoders. In *Proceedings of the 23rd ACM SIGKDD international conference on knowledge discovery and data mining*, pages 665–674, 2017. [2](#)
- [68] Kaichen Zhou, Yang Cao, Taewhan Kim, Hao Zhao, Hao Dong, Kai Ming Ting, and Ye Zhu. RAD: A dataset and benchmark for real-life anomaly detection with robotic observations. *CoRR*, abs/2410.00713, 2024. [2](#)
- [69] Qiang Zhou, Weize Li, Lihan Jiang, Guoliang Wang, Guyue Zhou, Shanghang Zhang, and Hao Zhao. PAD: A dataset and benchmark for pose-agnostic anomaly detection. In *Advances in Neural Information Processing Systems 36: Annual Conference on Neural Information Processing Systems 2023, NeurIPS 2023, New Orleans, LA, USA, December 10 - 16, 2023*, 2023. [1](#), [2](#), [8](#)
- [70] Qihang Zhou, Guansong Pang, Yu Tian, Shibo He, and Jiming Chen. Anomalyclip: Object-agnostic prompt learning for zero-shot anomaly detection. In *The Twelfth International Conference on Learning Representations, ICLR 2024, Vienna, Austria, May 7-11, 2024*. OpenReview.net, 2024. [2](#)
- [71] Yang Zou, Jongheon Jeong, Latha Pemula, Dongqing Zhang, and Onkar Dabeer. Spot-the-difference self-supervised pre-training for anomaly detection and segmentation. In *European Conference on Computer Vision*, pages 392–408. Springer, 2022. [1](#), [6](#)

Multi-Flow: Multi-View-Enriched Normalizing Flows for Industrial Anomaly Detection

Supplementary Material

6. Comprehensive Detection Results

We provide the full results for detection of all baselines on all classes of Real-IAD in Tab. 5 and Tab. 6.

Classes	PaDiM [12]	Cflow [21]	SoftPatch [26]	DeSTSeg [64]	RD [13]	UniAD [58]	PatchCore [48]	SimpleNet [38]	<i>Multi-Flow</i> (ours)
Audiojack	<u>92.2</u>	82.0	91.0	95.3	81.9	91.2	89.3	91.2	96.56 ± 0.12
Bottle Cap	98.1	98.8	99.1	92.4	93.7	97.3	99.4	99.4	98.00 ± 0.14
Button Battery	88.7	96.3	91.9	93.3	83.3	87.5	90.6	<u>95.8</u>	96.57 ± 0.16
End Cap	76.1	75.1	<u>92.3</u>	82.3	68.1	89.4	91.9	94.2	90.89 ± 0.09
Eraser	96.5	87.2	96.1	91.9	82.9	91.2	<u>95.6</u>	94.7	92.81 ± 0.14
Fire Hood	96.9	87	87.8	96.9	81.4	83.0	89.3	95.6	95.45 ± 0.10
Mint	69.1	79.1	82.1	77.7	67.7	73.0	85.7	<u>86.8</u>	87.84 ± 0.03
Mounts	98.4	98.2	99.3	99.1	92.5	97.0	99.7	99.4	99.46 ± 0.02
PCB	88.4	83.1	90.3	83.6	79.3	83.2	<u>93</u>	90.7	93.91 ± 0.11
Phone Battery	91.7	91.2	91.5	<u>98.2</u>	89.4	93.6	95.1	94.7	98.68 ± 0.06
Plastic Nut	<u>98.2</u>	88.6	95.7	<u>94.4</u>	72.8	87.1	97.8	95.7	98.96 ± 0.10
Plastic Plug	<u>87.4</u>	90.0	92.5	<u>95.6</u>	89.3	78.0	95.7	94.4	93.85 ± 0.07
Porcelain Doll	93.8	<u>95.1</u>	94.7	<u>94.6</u>	89.6	92.8	96.1	96.2	94.37 ± 0.42
Regulator	96.5	85.1	82.9	93.0	92.5	55.5	86.0	92.0	94.22 ± 0.22
Rolled Strip Base	98.6	98.8	99.7	98.9	80.3	99.3	99.7	<u>99.6</u>	99.57 ± 0.09
SIM Card Set	94.2	95.6	98.4	98.3	89.9	94.0	99.3	<u>99.2</u>	98.79 ± 0.04
Switch	82.1	92.9	97.8	96.6	87.3	95.3	94.6	<u>98.8</u>	99.27 ± 0.03
Tape	99.8	98.5	99.7	99.1	89.5	99.1	<u>99.9</u>	100	97.12 ± 0.12
Terminal Block	96.9	92.2	<u>98.2</u>	96.1	89.8	93.8	97.5	97.7	99.09 ± 0.02
Toothbrush	91.7	91.9	92.9	97.9	86.7	95.0	94.7	95.3	<u>96.88</u> ± 0.13
Toy	91.4	78.8	91.3	96.5	75.0	77.2	92.8	92.9	<u>96.46</u> ± 0.19
Toy Brick	84.3	82.9	78.2	<u>87</u>	72.5	78.3	82.6	85.7	91.73 ± 0.14
Transistor1	90.3	96.6	99.3	<u>99.0</u>	94.7	99.3	99.8	<u>99.7</u>	98.55 ± 0.07
U Block	98.3	96.7	98.3	<u>98.5</u>	86.9	96.3	98.8	<u>98.5</u>	96.57 ± 0.10
USB	77.0	86.1	93.8	<u>93.3</u>	89.4	83.1	<u>93.9</u>	<u>93.9</u>	96.83 ± 0.04
USB Adaptor	93.2	86.8	91.9	93.6	65.3	85.1	90.6	93.0	93.39 ± 0.18
Vcpill	94.7	87.8	93.7	96.4	87.2	89.4	<u>96.5</u>	97.5	95.90 ± 0.11
Wooden Beads	91.1	89.3	90.9	91.9	85	82.5	91.4	<u>92.9</u>	94.72 ± 0.16
Woodstick	81.8	83.9	73.9	90.2	71.9	76.0	74.5	81.5	89.15 ± 0.19
Zipper	99.3	97.6	99.6	99.7	96.1	98.8	100	99.7	<u>99.92</u> ± 0.00
Average	91.2	89.8	92.8	94.0	83.7	88.1	93.7	<u>94.9</u>	95.85 ± 0.02

Table 5. Performance in sample-wise anomaly detection on all classes of Real-IAD [54]. Here, the anomaly scores for all images belonging to the same object are aggregated into one value. Best performances are **bold**, with the runner-up underlined. We execute our method for $n = 5$ runs and report mean ± standard deviation.

Classes	PaDiM [12]	Cflow [21]	SoftPatch [26]	DeSTSeg [64]	RD [13]	UniAD [58]	PatchCore [48]	SimpleNet [38]	<i>Multi-Flow</i> (ours)
Audiojack	66.6	74.3	<u>88.5</u>	81.8	82.4	82.8	86.3	87.4	90.69 ± 0.06
Bottle Cap	87.7	91.3	95.9	87.1	89.2	89.8	94.3	91.6	<u>94.62</u> ± 0.14
Button Battery	84.8	85.2	88.5	91.2	87.0	79	87.3	88.8	<u>89.37</u> ± 0.16
End Cap	73.7	66.4	85.8	80.3	79.0	80.4	84.1	83.4	<u>84.77</u> ± 0.10
Eraser	86.7	88.1	93.5	88.2	89.2	89.6	<u>93.4</u>	91.2	<u>92.08</u> ± 0.11
Fire Hood	77.3	80.5	<u>84.3</u>	78.9	84.3	79.5	84.1	81.8	93.35 ± 0.13
Mint	66.9	70.7	<u>74.5</u>	70.5	<u>71.6</u>	67.6	76.2	<u>77.2</u>	79.38 ± 0.11
Mounts	82.5	85.3	85.9	85.1	85.7	87.2	<u>88</u>	88.2	84.26 ± 0.11
PCB	75.0	77.3	90.8	79.6	89.5	80.5	92.4	87.1	<u>91.79</u> ± 0.09
Phone Battery	81.9	84.4	90.2	86.2	<u>90.8</u>	83.4	91.6	88.9	<u>90.77</u> ± 0.35
Plastic Nut	73.8	79.8	89.3	<u>90.2</u>	85.0	79.3	90.8	89.3	88.04 ± 0.13
Plastic Plug	80.0	83.9	88.7	86.0	90.5	78.2	<u>89.7</u>	87.1	88.45 ± 0.11
Porcelain Doll	74.3	76.0	86.1	83.7	<u>87.8</u>	84.1	88.2	86.1	86.62 ± 0.23
Regulator	76.5	62.9	82.1	89.8	87.3	51.8	81.9	82.2	<u>87.69</u> ± 0.18
Rolled Strip Base	97.4	97.1	<u>99.1</u>	98.3	94.3	98.6	98.9	99.4	<u>98.15</u> ± 0.12
SIM Card Set	91.8	94.4	95.8	91.8	93.6	91.1	97.1	<u>96.1</u>	90.65 ± 0.16
Switch	80.8	83.9	94.7	92.5	87.2	85.7	89.4	<u>94.8</u>	96.03 ± 0.12
Tape	93.7	96.0	<u>97.9</u>	96.1	93.1	97.2	98.2	96.9	94.32 ± 0.11
Terminal Block	86.7	85.1	<u>96.2</u>	91.4	94.5	85.9	94.1	93.4	96.41 ± 0.19
Toothbrush	74.4	79.9	89.3	87.5	83.4	82.7	<u>88.0</u>	86.1	85.21 ± 0.17
Toy	82.5	67.8	86.7	82.1	81.5	67.3	<u>87.3</u>	82.2	88.31 ± 0.10
Toy Brick	71.0	80.7	79.8	76.8	73.9	77.9	<u>81.4</u>	80.8	87.35 ± 0.01
Transistor1	86.5	92.8	97.2	95.6	95.8	94.1	97.8	<u>97.3</u>	94.86 ± 0.14
U Block	84.1	90.5	91.6	90.1	<u>91.7</u>	88.8	91.9	90.7	90.45 ± 0.19
USB	69.7	78.1	91.2	90.3	<u>92.1</u>	80.9	90.7	90.0	93.37 ± 0.03
USB Adaptor	81.9	75.2	<u>86</u>	73.1	71.9	77.3	83.8	82.7	88.07 ± 0.13
Vcpill	67.4	85.8	89.6	90.0	90.2	88.6	91.4	<u>91.1</u>	89.50 ± 0.19
Wooden Beads	82.4	87.4	89.2	86.2	87.4	80.7	<u>88.6</u>	85.7	87.28 ± 0.05
Woodstick	79.9	78.9	76.0	89	84.2	78.9	<u>77.2</u>	77.9	88.04 ± 0.17
Zipper	90.4	93.8	97.9	88.4	97.8	98.2	98.1	<u>98.2</u>	98.23 ± 0.08
Average	80.3	82.5	<u>89.4</u>	86.9	87.1	82.9	<u>89.4</u>	88.5	90.27 ± 0.02

Table 6. Performance in image-wise anomaly detection on all classes of Real-IAD [54]. Here, the anomaly scores for all images belonging to the same object are aggregated into one value. Best performances are **bold**, with the runner-up underlined. We execute our method for $n = 5$ runs and report mean ± standard deviation.

Metrics	PaDiM [12]	Cflow [21]	SoftPatch [26]	DeSTSeg [64]	RD [13]	UniAD [58]	PatchCore [48]	SimpleNet [38]	<i>Multi-Flow</i> (ours)
AUPRO	81.8	90.5	90.8	81.5	93.8	86.1	<u>91.5</u>	84.6	87.91 ± 0.01
Pixel-AUROC	-	-	-	-	-	-	-	-	96.47 ± 0.00

Table 7. **Average** segmentation performance of various methods across all classes in Real-IAD [54]. Pixel-wise AUROC has not been reported for the baselines. Best performances are **bold**, with the runner-up underlined. We execute our method for $n = 5$ runs and report mean ± standard deviation.